- 1 Synthesis and SERS Application of Gold and Iron Oxide
- **2 Functionalized Bacterial Cellulose Nanocrystals**
- 3 (Au@Fe3O4@BCNCs)
- 4 Seju Kang,a,b,1 Asifur Rahman,a,b,1 Ethan Boeding,a,b Peter J. Vikesland,a,b*
- 5 aDepartment of Civil and Environmental Engineering, Virginia Tech, Blacksburg, Virginia;
- 6 bVirginia Tech Institute of Critical Technology and Applied Science (ICTAS) Sustainable
- 7 Nanotechnology Center (VTSuN), Blacksburg, Virginia;

8

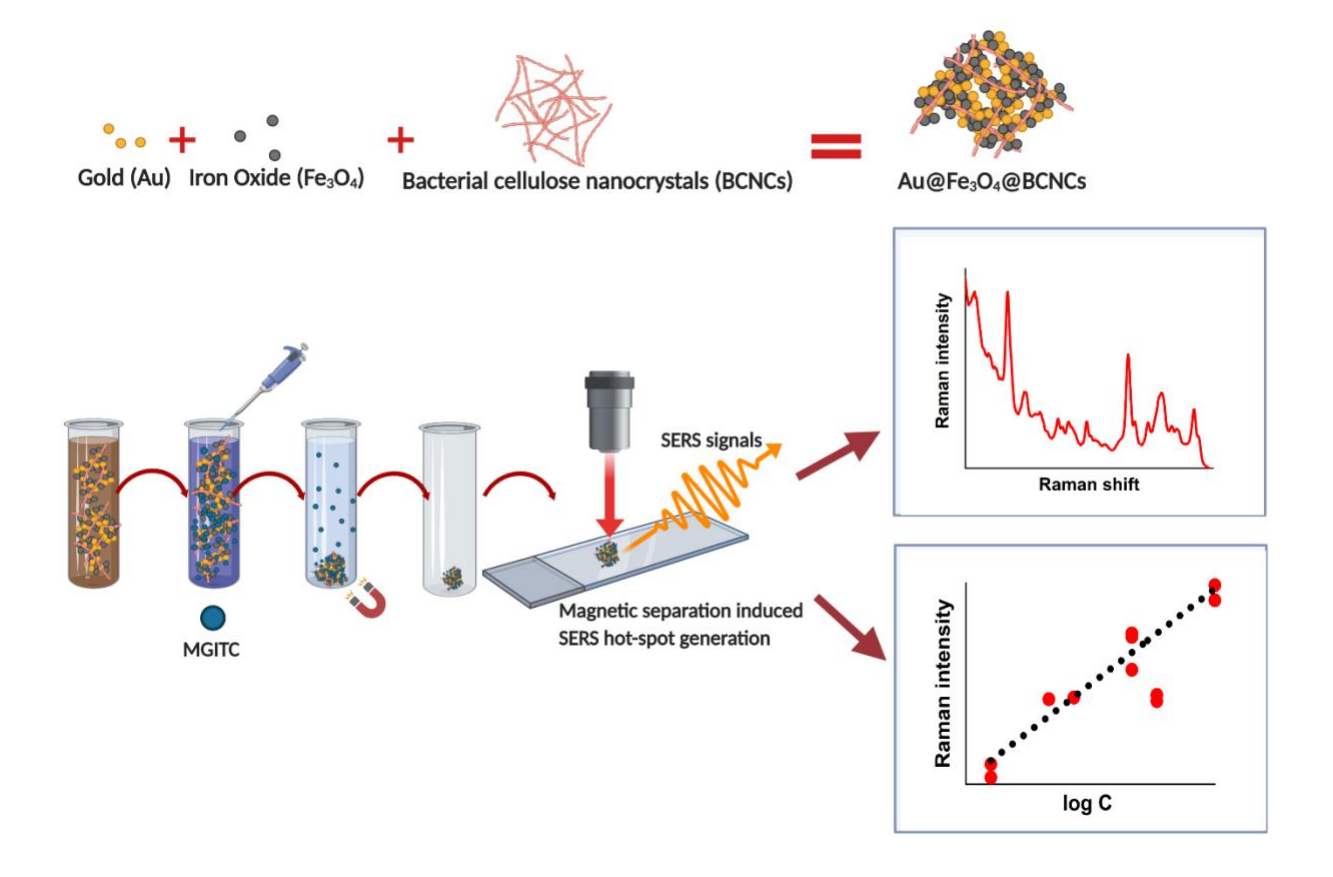
- 9 These authors made equal contributions to this work.
- 10 * Corresponding author: pvikes@vt.edu

11

Abstract

Bacterial cellulose nanocrystals (BCNCs) are biocompatible cellulose nanomaterials that can host guest nanoparticles to form hybrid nanocomposites with a wide range of applications. Herein, we report the synthesis of a hybrid nanocomposite that consists of plasmonic gold nanoparticles (AuNPs) and superparamagnetic iron oxide (Fe₃O₄) nanoparticles supported on BCNCs. As a proof of concept, the hybrid nanocomposites were employed to isolate and detect malachite green isothiocyanate (MGITC) via magnetic separation and surface-enhanced Raman scattering (SERS). Different initial gold precursor (Au₃₊) concentrations altered the size and morphology of the AuNPs formed on the nanocomposites. The use of 5 and 10 mM Au₃₊ led to a heterogenous mix of spherical and nanoplate AuNPs with increased SERS enhancements, as compared to the more uniform AuNPs formed using 1 mM Au₃₊. Rapid and sensitive detection of MGITC at concentrations as low as 10-10 M was achieved. The SERS intensity of the normalized Raman peak at 1175 cm-1 exhibited a log-linear relationship for MGITC concentrations between 2×10-10 and 2×10-5 M for Au@Fe₃O₄@BCNCs. These results suggest the potential of these hybrid nanocomposites for application in a broad range of analyte detection strategies.

29 Graphical abstract



Introduction

38

39

40

41

42

43

44

45

46

47

48

49

50

51

52

53

54

55

56

57

58

59

60

Bacterial cellulose (BC) is a cellulose nanomaterial synthesized by a number of bacterial species (i.e., Achromobacter, Alcaligenes, and Gluconacetobacter xylinus) in liquid culture media. 1-3 Due to its facile synthesis and biocompatibility, BC has great potential for environmental, biomedical, and drug delivery applications.4-7 Hydroxyl groups on the BC surface enable attachment of diverse types of nanoparticles and production of BC-based nanocomposites. BC substrates can be functionalized with iron oxide (Fe₃O₄) nanoparticles due to their high reactivity and capacity for magnetic separation.8-10 The facile synthesis and surface functionalization of BC with Fe₃O₄ nanoparticles enables catalytic, biomedical, drug delivery and magnetic resonance imaging (MRI) applications. 11, 12 In addition, gold nanoparticle (AuNP) functionalized BCs have potential applications as biosensors. AuNPs can be synthesized and deposited onto BC substrates for analyte detection.3, 13 Adjacent plasmonic metal nanoparticles with nano-sized gaps enhance inelastic Raman scattering signals due to the localized surface plasmon resonance effect – this phenomenon makes surface-enhanced Raman spectroscopy (SERS) possible. 14, 15 The high Raman enhancement factors (104 to 1012) of SERS makes it a promising technique for highly sensitive detection (<ng L-1).16, 17 The development of SERS substrates to optimize the Raman signal is a highly interesting and active research area. Colloidal nanoparticles immobilized on cellulose substrates are of growing interest because of the cost-effective preparation and scalability of the approach.3, 18, 19 Following strong acid hydrolysis of BC, bulk cellulose can be converted into highly crystalline cellulose fragments commonly referred to as bacterial cellulose nanocrystals

(BCNCs).20 The use of BCNCs is advantageous due to their high specific surface area, colloidal

and thermal stability, high tensile strength, and nanometric dispersity, 2, 21, 22 In a recent study,

cationic BCNCs coated by amines and amine-containing polymers were developed as nucleic acid nanocarriers.23 Recently researchers developed hydroxypropyl methylcellulose combined with BCNCs and silver nanoparticles to improve the tensile strength of a product potentially useful to the food packaging industry.24

61

62

63

64

65

66

67

68

69

70

71

72

73

74

75

76

77

78

79

80

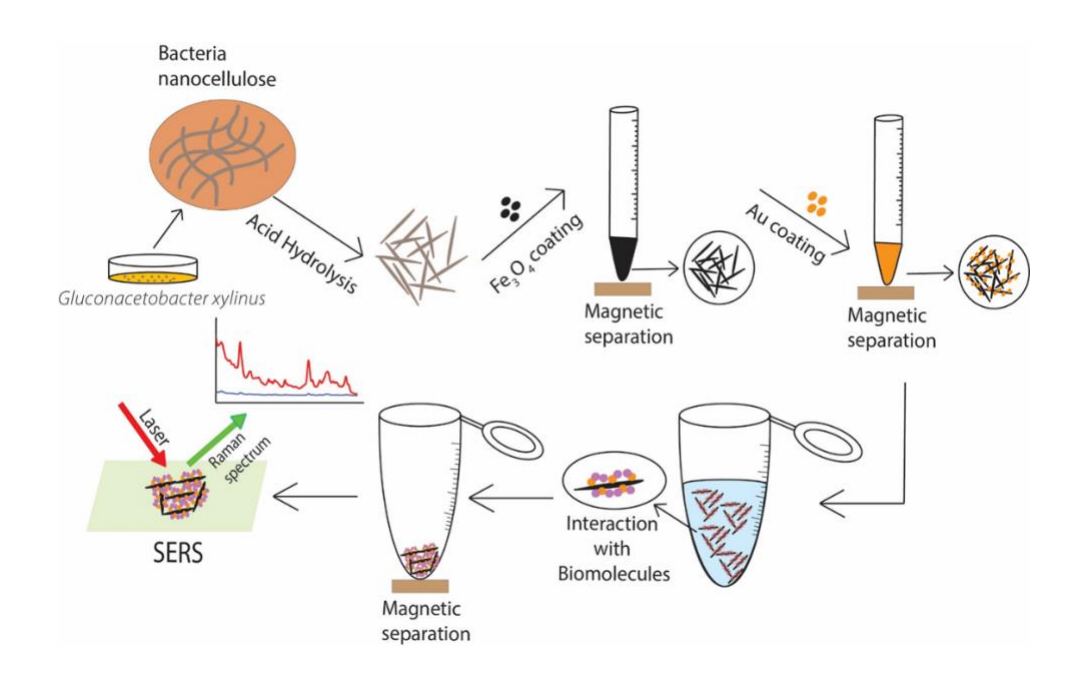
81

82

In this study, we report the facile synthesis of hybrid BCNC-based nanocomposites coated with AuNPs and Fe₃O₄ nanoparticles (Au@Fe₃O₄@BCNCs). Fe₃O₄ nanoparticles were synthesized from an iron precursor dissolved in BCNC suspension and immobilized in situ onto the BCNCs to form Fe₃O₄ nanoparticle coated BCNCs (Fe₃O₄@BCNCs). This step was followed by the *in situ* reduction of Au₃₊ in the presence of Fe₃O₄@BCNCs to produce Au@Fe₃O₄@BCNCs. Previously, Au and Fe₃O₄ nanoparticles were combined in Au shell- Fe₃O₄ core materials and Au-Fe heterodimers for application in target molecule binding and detection through optical SERS sensing 25, 26 The production of core-shell nanoparticles exhibits many challenges such as the poor diffusion barrier of the core layer due to shell formation, difficulties in controlling the uniformity and thickness of the shell coating, and atomic lattice mismatches between the core and shell components.25, 27, 28 BCNCs can potentially be used as alternative substrates that can readily bind to guest metals such as Au and Fe₃O₄ nanoparticles through C=O-metal binding or electrostatic interactions.4, 21 Fe₃O₄@BCNCs can be quickly separated from suspension and can be used to concentrate target molecules using an external magnetic field. Furthermore, Fe₃O₄ nanoparticles can be easily detached from BCNCs following strong acid treatment and the BCNCs can then be re-functionalized, making them environmentally friendly. The Fe₃O₄@BCNCs can be further functionalized with AuNPs to utilize the biocompatibility and plasmonic nature of AuNPs. The Au@Fe₃O₄@BCNC platform combines the magnetic separation capability of Fe₃O₄ nanoparticles

and SERS-active AuNPs for interaction with and SERS detection of organic molecules (**Scheme** 1).

The hybrid BCNC-based nanocomposites developed in this study were comprehensively characterized using transmission electron microscopy (TEM), scanning electron microscopy (SEM) and electrophoretic mobility measurements. As a proof-of-concept, we investigated the efficacy of the nanocomposites for the detection of malachite green isothiocyanate (MGITC) by SERS with different initial concentrations of Au₃₊ for functionalization.



Scheme 1. Schematic illustration of synthesis, functionalization, and SERS application of the Au@Fe₃O₄@BCNCs

Materials and Methods

Materials

Gold chloride trihydrate (HAuCl₄·3H₂O, ≥99.9%), sodium citrate tribasic dihydrate (Na₃Cit.2H₂O, ≥99.0%), fructose, yeast extract, calcium carbonate (CaCO₃, Reagent Plus), ammonium hydroxide (NH₃OH, ACS Reagent, 28-30% NH₃ basis), and iron(II) chloride (98%) were obtained from Sigma-Aldrich (St. Louis, MO, USA). Sodium hydroxide (NaOH, certified ACS), hydrochloric acid (HCl, certified ACS plus), ferric chloride hexahydrate (FeCl₃.6H₂O, certified ACS) and malachite green isothiocyanate (MGITC) were purchased from Thermo Fisher Scientific (Hampton, NH, USA). Deionized (DI) water was ultrapure with ≥ 18 MΩ cm resistance.

Synthesis of BC pellicles followed by BCNC preparation

BC pellicles in petri dishes were synthesized following a published approach with minor revision.3 The cellulose-producing bacterial strain *Gluconacetobacter xylinus* (*G. xylinus*) was used to produce the BC pellicles. Prior to inoculating with *G. xylinus*, all media was autoclaved at 121 °C and 15 psi for 20 mins. Approximately 10 mL aliquots of ATCC medium 459 (10 g fructose, 1 g yeast extract, and 2.5 g CaCO3 in 200 mL of DI water) were poured into 100 mm diameter, 15 mm deep petri dishes. One or two visible *G. xylinus* colonies that had formed on nutrient agar were scooped and inoculated into each ATCC medium. This inoculated medium was quiescently stored in a 303 K oven for five days. After five days of incubation, hydrogel-like BC pellicles were generated. These pellicles were removed and rinsed using tap water to remove residual bacterial cells and nutrients. Following this cleaning, the BC pellicles were immersed in 0.1 M NaOH and stirred for three days to remove remaining residuals and hinder additional cellulose production. The cleaned BC pellicles were stored in DI water at room temperature until use.

To prepare a BCNC suspension, a single piece of BC pellicle was hydrolyzed with 10-15 mL of 37 % (w/w) HCl solution at 80°C for 3.5 hours under continuous stirring. The acid hydrolysis reaction was then terminated and 40 mL of DI water was added to the reaction flask. The resulting cloudy and acidic BCNC suspension was centrifuged at 4,000 rpm for 30 mins. After centrifugation, the sediment was collected and re-suspended in DI water. This cycle was repeated until the pH of the BCNC suspension was between 6-7.

Functionalization with Fe₃O₄ nanoparticles and AuNPs

The BCNCs were centrifuged and mixed in 20 mL of DI water containing FeCl₃·6H₂O and FeCl₂ in a 2:1 molar ratio. The mixture was transferred to a round bottom flask and was purged with N₂ gas for 1 hour while being magnetically stirred at 600 rpm. The suspension was then heated to 80 °C in a silicone oil bath and 5 mL of NH₄OH (28-30%) was added dropwise using a syringe. Upon addition of NH₄OH, the color of the suspension changed from orange/yellow to black, which indicated the attachment of Fe₃O₄ nanoparticles onto the BCNCs. The suspension was stirred for 30 mins and then cooled to room temperature. The cooled suspension was diluted to 50 mL in DI water and was repeatedly washed and magnetically separated until excess Fe₃O₄ nanoparticles were fully removed. These magnetic separations were performed using a neodymium disc magnet (N52, 40×20 mm). Finally, the Fe₃O₄@BCNCs were stored in 50 mL of DI water.

To functionalize Fe₃O₄@BCNCs with AuNPs, 5 mL aliquots of Fe₃O₄@BCNC suspension were transferred into a conical tube. A magnetic field was applied to separate the nanocomposites. The supernatant was decanted and replaced with a fixed 5 mL volume of either 1, 5, or 10 mM HAuCl₄. To accelerate the reduction of Au₃₊ to AuNPs, Na₃Cit was added as a reducing agent. For each HAuCl₄ concentration, small aliquots of Na₃Cit (~ 200 μL) were added into the samples at a 1:1 molar ratio of HAuCl₄ and Na₃Cit. The samples were then incubated at 303 K overnight. The

yellow Au₃₊ suspension rapidly changed to brown indicating the reduction of Au₃₊ to AuNP. The samples were repeatedly washed with DI water by magnetic separation and re-suspension until the supernatant became transparent indicating the removal of non-deposited AuNPs.

Characterization of the Au@Fe3O4@BCNCs

139

140

141

142

143

144

145

146

147

148

149

150

151

152

153

154

155

156

157

158

159

160

161

TEM was used to observe the morphology of the BCNCs, Fe₃O₄@BCNCs, and Au@Fe₃O₄@BCNCs. The as-synthesized BCNC suspension $[(\sim 0.01\% \text{ (w/v)}]]$ was deposited on a carbon mesh 200 grid (Ted Pella, Inc; Redding, CA), dried, and negatively stained with 2% uranyl acetate solution. The Fe₃O₄@BCNCs and Au@Fe₃O₄@BCNCs were diluted 10× and 10 μL of each sample was deposited onto the TEM grid without staining because negative staining can affect the imaging of Au and Fe₃O₄. TEM analysis was conducted using a field emission gun instrument (JEOL 2100) operating at an accelerating voltage of 200 kV. Nanoparticle sizes in each sample were determined (n=50) using ImageJ software. The morphologies of AuNPs on the Au@Fe3O4@BCNCs were characterized using a field-emission Quanta 600 FEG environmental SEM. Secondary electron (InLens detector) mode was used to obtain contrast between aggregated BCNCs and AuNPs, while backscattered electron (RBSD detector) mode was used for energy dispersive spectroscopy (EDS) mapping and analysis. To compare the surface charge and stability of the different nanocomposites, electrophoretic mobility (UE, m2Vs-1) was measured using a Zetasizer Nano DLS (Malvern Nano ZS, Malvern, UK). UE indicates particle response to an applied electric field and is measured by doppler frequency shifts in scattered light.

Proof-of-concept SERS application of the Au@Fe3O4@BCNCs

For the detection experiment, MGITC was selected because it has a large Raman cross-section and high affinity to the AuNP surface due to its thiol group.29, 30 In a 2-mL tube, different concentrations of 500 μ L MGITC solution were added into 500 μ L of Au@Fe₃O₄@BCNC

suspension. Following 3-4 hours of incubation at room temperature, the nanocomposites were magnetically separated and the supernatant was decanted. A preliminary test of sorption kinetics for MGITC was conducted by using the UV-Vis spectrophotometer. This test indicated that sorption reached equilibrium approximately within 2 hours (**Figure S1**). The residue was resuspended using $10~\mu L$ of DI water and pipetted onto a glass slide. Raman spectra were collected using a WITec alpha500R Raman spectrometer (WITec GmbH, Ulm, Germany, spectral resolution = \sim 3.5 cm-1), with a 785-nm laser (5 mW intensity) and a $10\times$ confocal microscope objective. The signal was collected using a Peltier cooled charge-coupled device (CCD) with 300 groves per mm grating set. For each sample, a total of 20×20 points (X \times Y) were acquired across a $10\times10~\mu m2$ area with 0.1 s integration time for each point.

SERS data analysis

For the collected Raman spectra, the baselines were corrected using an asymmetric least square smoothing method coded through Mathworks MATLAB/SIMULINK software (ver. R2019b). After baseline correction, the Raman intensities of the peaks of interest at 1175 and 77 cm-1 (I1175 and I77) were extracted and the intensity ratio of the peaks (I1175/I77) was plotted against the logarithm of MGITC concentrations.

To calculate the limit of detection (LOD) of the Au@Fe₃O₄@BCNCs, the best-fit regression line was determined as follows,

180
$$I_{1175}/I_{77} = \hat{a} \log C + \hat{b}$$

where \hat{a} and \hat{b} are the slope and y intercept of the regression line. The LOD was calculated using the following the equation,

$$\log LOD = (3\sigma_{\hat{a}} - \hat{b}) / \hat{a}$$

 $\sigma_{\hat{a}}$ is the standard deviation of the slope of the regression line.

Results and Discussion

Synthesis and characterization of the nanocomposites

TEM images of the as-synthesized BCNCs revealed rod or needle shaped structures 30-40 nm in width and 400-800 nm in length (**Figure 1A**). We did not perform post-treatment steps such as dialysis or filtration on the BCNC samples and this explains the presence of some impurities in the sample. The morphologies of the HCl-hydrolyzed BCNCs in this study are similar to those reported previously by Singhsa et. al.23 HCl-hydrolysis has been reported to produce cellulose nanocrystals (CNCs) in greater yield and larger dimensions relative to H2SO4-hydrolysis.23, 31 Given that the charged SO42- groups from H2SO4 can compromise the thermostability of the nanocrystals, HCl is thought to better optimize the CNC hydrolysis conditions.31, 32

The Fe₃O₄@BCNCs were prepared by the *in situ* synthesis of Fe₃O₄ nanoparticles on the BCNCs. Upon attachment of Fe₃O₄ nanoparticles, the Fe precursor/BCNC solution turned black indicating the formation of Fe₃O₄ nanoparticles. Following synthesis, the Fe₃O₄@BCNCs could be completely separated from suspension within 5 mins using a magnetic field (40×20 mm N52 neodymium disc magnet) (**Figure 1B**). AuNP functionalization of Fe₃O₄@BCNCs was done by the *in situ* reduction of Au₃₊ using Na₃Cit as reducing agent. Na₃Cit is a widely used reducing agent that accelerates AuNP formation.₃, ₃₃ Upon AuNP formation, the color of the Au@Fe₃O₄@BCNC suspension changed from black to dark brown suggesting a higher reduction capacity of Na₃Cit compared to the BCNC-OH surface functional groups as reported previously (**Figure 1D**).₃

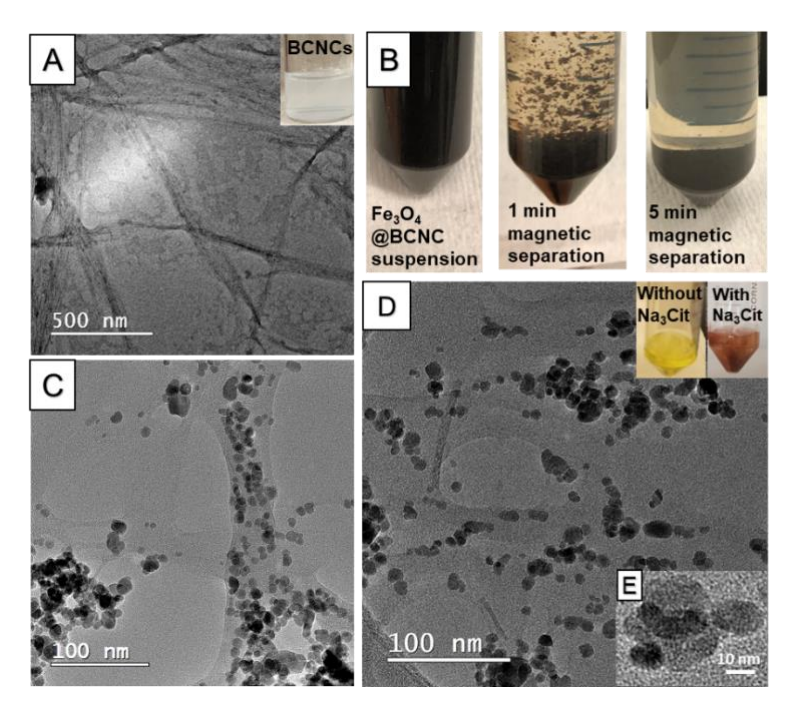


Figure 1. (A) TEM image of as-synthesized BCNCs (B) Fe₃O₄ coated BCNCs in suspension and magnetically separated (C) TEM image of Fe₃O₄@BCNCs, (D) TEM image of Au@Fe₃O₄@BCNCs and (E) Au and Fe₃O₄ nanoparticles.

FT-IR analysis of the BCNCs, BCNCs with Fe precursor, Fe₃O₄@BCNCs and Au@Fe₃O₄@BCNCs were performed to analyze the nature of the chemical bonding of BCNCs with nanoparticles. In the presence of Fe precursors and after Fe₃O₄ nanoparticle formation via Fe reduction, the peak at around 3340 cm-1 (BCNC-OH group) did not show any major shift (**Figure S2A**). This result suggests limited Fe-OH binding to the BCNC surface and an apparent electrostatic interaction between the -OH and Fe+3 seems to govern the interactions between BCNC-OH and Fe₃O₄ nanoparticles.₂₁, ₃₄, ₃₅. FT-IR spectra of the Au@Fe₃O₄@BCNCs had similar peaks to the uncoated BCNC sample. All samples had characteristic FT-IR peaks at 3345 cm-1, the O-H stretching vibration, and at 1640 cm-1, attributed to -OH groups of adsorbed water (**Figure S2**).₂₁, ₃₆ Other identified peaks were at 2896 cm-1 (C-H stretching) and 1060-1162 cm-1 (C-O and

C-O-C stretching bonds in BCNC), suggesting no significant degradation of the BCNCs during Au and Fe₃O₄ functionalization (**Figure S2**).

The morphologies of the nanoparticles within the Fe₃O₄@BCNCs and the Au@Fe₃O₄@BCNCs were characterized using TEM. Figures 1C and 1D show the typical morphology of the Fe₃O₄@BCNCs and the 5 mM Au@ Fe₃O₄@BCNCs nanocomposites, with Au typically showing higher contrast (Figure 1E). The as-synthesized BCNCs were stained with 2% uranyl acetate before TEM imaging and hence showed higher contrast (Figure 1A) compared to the unstained Au and Fe₃O₄ functionalized BCNCs (Figures 1C, 1D). The average nanoparticle diameter in the Fe₃O₄@BCNC samples was 9.43 ± 3.45 nm (n=50). After treatment with 5 mM Au₃₊, the average nanoparticle size increased to 11.75 \pm 2.4 nm (n=50). To better differentiate between the Au and Fe₃O₄ nanoparticles, we performed backscattered electron imaging and EDS analysis on magnetically separated and aggregated BCNC samples. As shown in Figure 2 (A to D), backscattered SEM images revealed an increased presence of Au on the aggregated Fe₃O₄@BCNC surface with an increase in initial Au precursor loading. An increase in the initial Au3+ concentration, from 1 to 5 mM caused formation of increased numbers of dispersed AuNPs. A further increase in Au₃₊ concentration to 10 mM caused the scattered formation of aggregated AuNPs and Au nanoplates. Previously, Wei et. al. observed Au nanoplate formation in AuNP coated BC substrates with Au₃₊ concentrations of 10 mM or higher.₃ In addition, EDS mapping of the aggregated 10 mM Au@Fe₃O₄@BCNC sample (**Figure 2, E-G**) suggested plate-like AuNPs. EDS spectra (Figure 2H) of an AuNP nanoplate (Figure 2E, point 1) showed a higher mass percent (42.88%) of Au compared to Au (2.86 mass %) directly associated with Fe₃O₄ nanoparticles (Figure 2E, point 2).

220

221

222

223

224

225

226

227

228

229

230

231

232

233

234

235

236

237

238

239

240

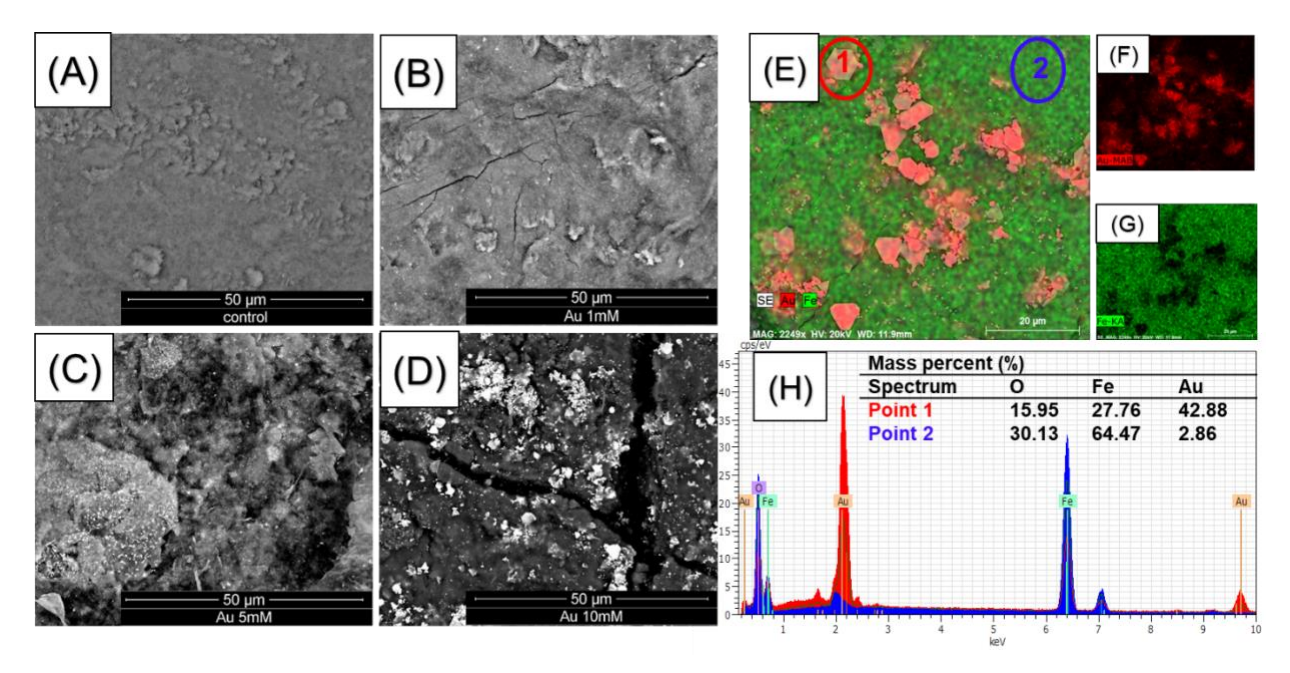


Figure 2. Backscattered SEM images of the aggregated (A) Fe₃O₄@BCNCs, (B) 1 mM Au@Fe₃O₄@BCNCs, (C) 5 mM Au@Fe₃O₄@BCNCs and (D) 10 mM Au@Fe₃O₄@BCNCs. EDS mapping of (E) 10mM Au@Fe₃O₄@BCNCs with (F) Au and (G) Fe elements highlighted. The corresponding (H) EDS spectra of the map are provided with mass percent of O, Fe, and Au shown.

Magnetic separation of the Au@Fe₃O₄@BCNCs in suspension induces nanocomposite aggregation, which can potentially form aggregated structures (**Figure 2E**). Aggregated AuNPs and Au nanoplates are typically characterized by strong SERS enhancements.₃, ₃₇, ₃₈ Magnet induced aggregation has been used previously for core-shell Au@Fe₃O₄ nanoparticles to produce interparticle "hot-spots" that can amplify the Raman signals to achieve highly-sensitive detection.₂₆

The effect of surface functionalization by Au and Fe₃O₄ on the electrophoretic mobility of the BCNCs is shown in **Figure 3**. The pH_{IEP} of the samples was estimated based upon where the

electrophoretic mobility goes to zero as a function of solution pH in 0.01 M NaCl suspensions. HCl-hydrolyzed BCNCs exhibited a strongly negative surface potential and were stable in NaCl suspension. At higher electrolyte (NaCl) concentrations of 0.025M or more, CNCs are reported to aggregate with a concomitant increase in hydrodynamic diameter.39 Upon functionalizing with Fe₃O₄ nanoparticles, the electrophoretic mobility for the Fe₃O₄@BCNCs was similar to that of bare Fe₃O₄ nanoparticles. This result contrasts with the unfunctionalized BCNCs, which showed mostly negative surface charge between pH 2 to 10. The pHiep of the Fe₃O₄@BCNCs was estimated to be 5.9, similar to bare Fe₃O₄ nanoparticles. After functionalizing with 1 and 10 mM Au₃₊, the pH_{IEP} of the nanocomposites shifted to between pH 3 and 4. Upon AuNP formation, the Au@Fe₃O₄@BCNCs showed negative surface charge at or above pH 4, similar to the observations in previous studies for Au nanoshell bearing cellulose nanocrystals and AuNPs.40, 41 Attachment of Au and Fe₃O₄ nanoparticles onto the BCNCs was carefully controlled to utilize the efficiency of both the magnetic and plasmonic properties of the hybrid nanocomposites. The electrophoretic mobility measurements suggest that using the stated amount of Fe and Au precursors, the resulting nanocomposites showed charge stability in suspension and minimal aggregation at a low salt concentration of 0.01 M NaCl.

258

259

260

261

262

263

264

265

266

267

268

269

270

271

272

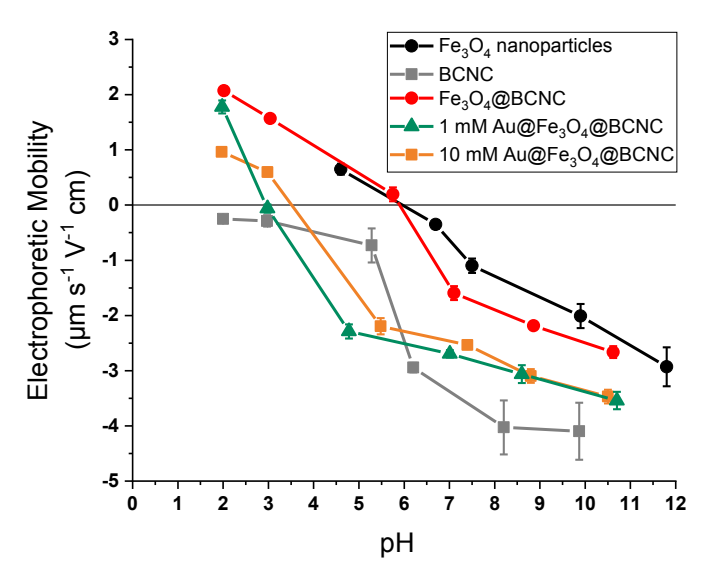


Figure 3. Electrophoretic mobility of bare Fe₃O₄ nanoparticles, BCNCs, Fe₃O₄@BCNCs, 1 mM and 10 mM Au@Fe₃O₄@BCNCs in 0.01 M NaCl solution. The error bars indicate standard deviation of three measurements.

SERS detection of MGITC using the nanocomposites

Using the Au@Fe₃O₄@BCNCs, SERS detection of MGITC was rapid and sensitive. Following sorption of MGITC to the nanocomposites, we readily separated the MGITC-sorbed nanocomposites from the suspension using a magnetic field. Within a few minutes, the suspension became transparent and the nanocomposites were concentrated near the magnet. Once the transparent supernatant was decanted, the nanocomposites were re-dispersed in 10 μL of DI water. After deposition of 10 μL of the droplet including the MGITC-sorbed nanocomposite onto the glass slide, we successfully collected the SERS spectra with several distinct peaks under both dry and wet conditions (**Figure 4A**). The occurrence of a peak at 215 cm-1 corresponding to the Au–S bond demonstrates the successful complexation of isothiocyanate (–N=C=S) in MGITC to the AuNP surface.₃₀ The most prominent peaks at 1175, 1366, and 1589 cm-1 can be assigned to the

n-plane benzene v₉ mode, the aromatic ring stretching mode, and the in-plane aromatic ring stretching/bending mode, respectively.₄₂, ₄₃ Other distinct peaks such as 914, 1296, and 1618 cm-1 arise from the B_{1u} in-plane benzene ring mode, in-plane C-H or C-C-H bending mode, and phenyl-N stretching mode.₄₂, ₄₃

In **Figure 4A**, insets show the pictures of the Au@Fe₃O₄@BCNCs in the dry and wet states. The coefficients of variance (CV) of the SERS band at 1175 cm-1 across the scanning area in both states were 13.8 and 14.0%, respectively (**Figure S3**). This result demonstrates that both conditions had low spatial variability. For the dry sample, it was quickly dried within ~5 mins in the oven at 60 °C. The collection time of the SERS spectra across a 10 μ m × 10 μ m area for one sample is only 40 s for 400 points in this study. The short intervals among analyte contact, sample separation, and data collection illustrate the rapid detection of MGITC using the Au@Fe₃O₄@BCNCs.

The overall SERS signals in a dry state were ~ 20 times higher than in the wet state (**Figure 4A**). After the droplet was dried, the Au@Fe₃O₄@BCNCs were densely packed at the edge due to the coffee ring effect and the distance between AuNPs became closer resulting in the formation of denser SERS hot-spots, especially at the edge. Additionally, we applied a magnetic field to the deposited droplet of the suspended MGITC-sorbed nanocomposites before drying to investigate if SERS intensities could be further enhanced (**Figure S4**). However, there was no significant effect on SERS enhancement, implying that the concentrated nanocomposites via the initial magnetic separation from suspension predominantly affected generation of SERS hot-spots. Hereafter, all SERS spectra were collected in the dry state due to its higher SERS enhancement.

The effect of the initial concentration of Au₃₊ during the functionalization experiments on the SERS performance of Au@Fe₃O₄@BCNC was investigated. **Figure 4B** shows the SERS spectra of 2 µM MGITC using Au@Fe₃O₄@BCNCs with different Au coating concentrations (1,

5, and 10 mM). It was observed that the peak intensities corresponding to MGITC increased with an increase in the initial concentration of Au₃₊. The SERS enhancement depends on the density, size, and morphology of AuNPs on the nanocomposite.³ The nanocrystals in our study provided more favorable SERS hot-spots with a higher initial concentration of Au₃₊. This observation may be attributed to the relatively larger size and quantity of AuNPs and formation of Au nanoplates, as observed in the SEM analysis (**Figure 2E**). The heterogenous morphologies of plasmonic Au metals present on the BCNCs can potentially improve SERS enhancement.³⁷, ³⁸

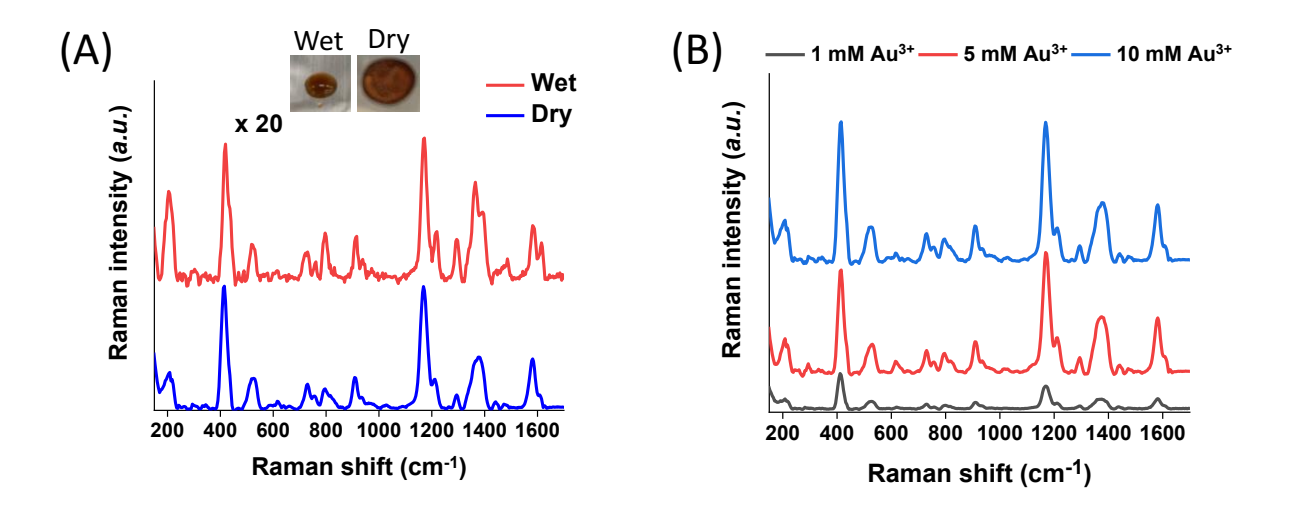


Figure 4. (A) Comparison of the SERS spectra of 2 μ M MGITC under wet and dry conditions using 10 mM Au@Fe₃O₄@BCNCs. Inset pictures show before/after drying of 10 μ L of the droplet including the nanocomposites (B) The SERS spectra of 2 μ M MGITC using the Au@Fe₃O₄@BCNCs with different Au coating condition (1, 5, and 10 mM Au₃₊). All spectra shown here are the average of 400 collected spectra.

Quantification of MGITC using SERS

We successfully detected MGITC with concentrations ranging from 2×10-5 to 2×10-10 M using the Au@Fe₃O₄@BCNCs. However, quantification was challenging due to the large variation in the spatial arrangement of heterogenous SERS hot-spots among the batches arising from random

aggregation of the nanocomposites. Therefore, we normalized the SERS hot-spots between different batches by using the intensity of the 77 cm-1 pseudo-peak (I77) as the internal standard. As discussed previously, I77 reflects elastically scattered light from the amplified spontaneous emission (ASE) of the Raman laser cut by the edge filter. In previous studies, it was reported that the density of SERS hot-spots can be reflected by the variation of I77,44-47 Figure 5A shows vertically stacked SERS spectra of different concentrations of MGITC using 1 mM Au@Fe3O4@BCNCs relative to a nanocomposite only control. All SERS spectra were averaged from 400 individual spectra and normalized by I77. It is noteworthy that the normalized intensities of the peaks were higher for higher concentrations of MGITC. For quantification, among many prominent peaks, the strongest peak at 1175 cm-1 was selected as representative.48,49 For each of the 1, 5, and 10 mM Au₃₊ coating conditions, the normalized Raman intensities at 1175 cm-1 (I1175/I77) were plotted against the logarithm of the MGITC concentration (Figure 5B-D). A linear relationship between Raman intensity and the logarithm of analyte concentrations is commonly observed in quantitative analysis of plasmonic nano-substrates.50-52 We suggest that hot-spot normalized Raman intensities further enhance quantification and account for the spatial heterogeneity of AuNPs. These plots showed a clear linear trend between the two variables in a certain range with R-squared values between 0.76 – 0.96. The lowest intensities of MGITCcorresponding peaks were observed at ~10-10 M for 1 and 5 mM Au@Fe3O4@BCNCs. On the other hand, no distinct peaks were detected at <10-8 M for 10 mM Au@Fe3O4@BCNCs which may be attributed to the decreased surface area of AuNP or Au nanoplate for MGITC sorption. Surprisingly, the Au@Fe3O4@BCNCs at the lower initial concentration of Au3+ tended to have a larger capacity for MGITC and ultimately higher detection sensitivity despite lower SERS enhancement. The sorption capacity of the Au@Fe3O4@BCNCs for MGITC depends on the

330

331

332

333

334

335

336

337

338

339

340

341

342

343

344

345

346

347

348

349

350

351

surface area of Au regarding the strong Au-S bond between them. A higher fraction of AuNPs at the lower initial concentration of Au₃₊ would provide a larger Au surface area, resulting in greater sorption capacity for MGITC than plate-like Au at higher concentration.

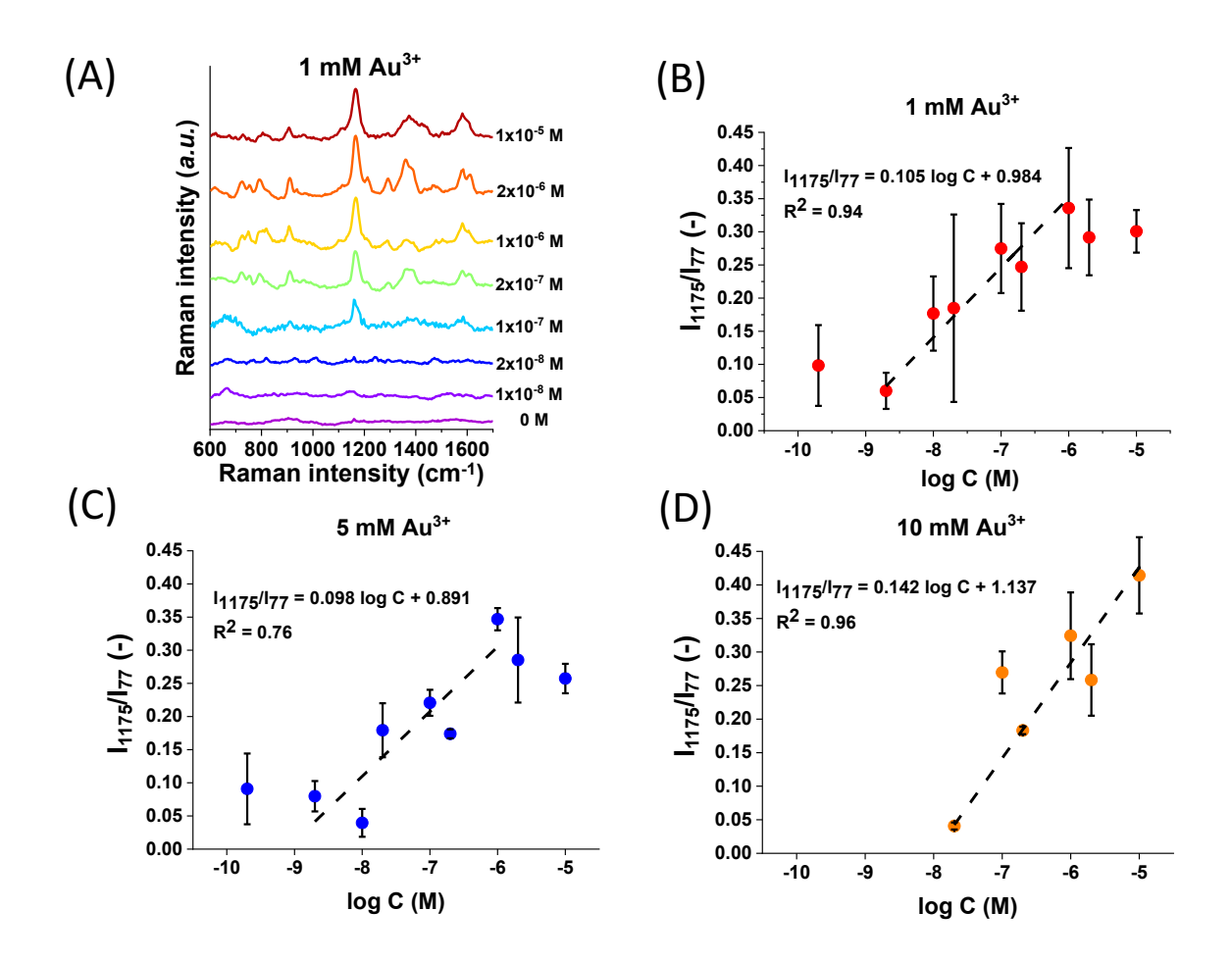


Figure 5. SERS detection of MGITC using the Au@Fe₃O₄@BCNCs (A) The SERS spectra of MGITC with the different concentrations using 1 mM Au@Fe₃O₄@BCNC stacked vertically for clarity (B)-(D) The plots of the normalized peak of 1175 cm-1 (I₁₁₇₅/I₇₇) vs the logarithm of concentrations of MGITC using 1, 5, and 10 mM Au@Fe₃O₄@BCNCs. Symbol and error bar represent the average and standard deviation of 400 spectra for each point, respectively.

The linear regression between the normalized I₁₁₇₅ and the logarithm of the concentration of MGITC was evaluated for all the Au@Fe₃O₄@BCNCs. The range of concentrations was restricted to the range from 2×10-9 to 2×10-6 M and the data points with responses comparable to the blank were omitted. The results shown in **Figure 6** suggest that the normalized I₁₁₇₅ can be reasonably approximated as a linear function of the logarithm of the MGITC concentration. The two parameters were statistically correlated with an R-square value of 0.79 and the experimental data were within the 95% prediction region. Using this approach, the LOD was determined to be 5.8×10-10 M from the empirical best-fit equation (i.e., I₁₁₇₅/I₇₇ = 0.837 + 0.087 log C) and the standard error of the regression.₅₃ We expect that it will be possible to further lower the LOD value by adjusting the size and morphology of AuNPs. Overall, this result demonstrates the applicability of Au@Fe₃O₄@BCNCs for quantitative SERS analysis.

We believe that tuning the Au and Fe₃O₄ nanoparticles in the experiment can improve the SERS performance of the Au@Fe₃O₄@BCNCs along with their magnetization capability in an interactive manner. In a previous study, core-shell Au-coated Fe₃O₄ nanoparticles showed a substantial reduction of the saturation magnetization compared to the bare Fe₃O₄ nanoparticles which may be attributed to the shielding effect of the Au layer on the outer side of magnetite.54 Further research on optimization of experimental functionalization conditions is required for these hybrid nanocomposites to expand their applicability.

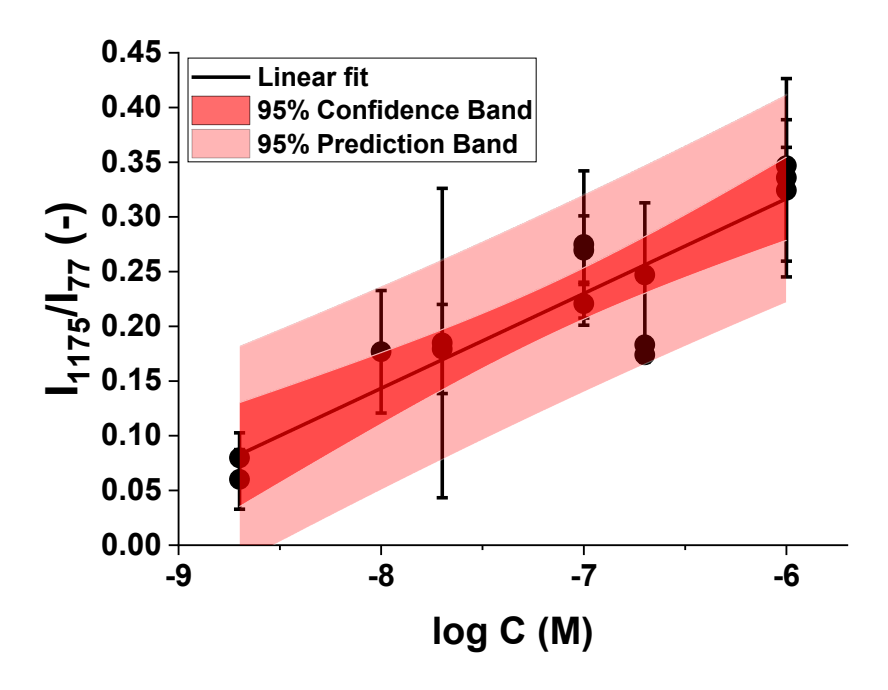


Figure 6. The comprehensive plot of the normalized Raman peak of 1175 cm-1 vs. the logarithm of the concentrations of MGITC using 1, 5, and 10 mM Au@Fe₃O₄@BCNCs. The black solid line shows the best-fit linear curve. Dark and light red-colored regions show statistical 95% confidence and prediction bands, respectively. $R_2 = 0.79$, Linear fit: $I_{1175}/I_{77} = 0.837 + 0.087 \log C$.

Conclusions

In this work, BCNCs were prepared by HCl hydrolysis of BC pellicles. The hybrid BC-based nanocomposites, Au@Fe₃O₄@BCNCs, were prepared by the sequential *in situ* synthesis of Fe₃O₄ and AuNPs in the presence of BCNCs. The efficacy of the hybrid nanocomposites as biomolecule binding and detection agents was evaluated through SERS detection of MGITC as a proof-of-concept. The structure of the BCNCs was unaffected after functionalizing with Fe₃O₄ and AuNPs. The size and morphology of AuNPs on the BCNCs were affected by the initial concentration of Au₃₊. The formation of heterogenous mixtures of aggregated AuNPs and Au nanoplates at high Au₃₊ concentration could be responsible for high SERS intensity. Magnetic

separation-induced generation of SERS hot-spots from the aggregated Au@Fe₃O₄@BCNCs had low spatial variability under both wet and dry conditions. Different concentration levels of MGITC were quantified through linear relationship between the normalized Raman peak of 1175 cm-1 vs. the logarithmic concentrations of MGITC. These results suggest that the Au@Fe₃O₄@BCNCs used in this study have great potential for biomolecular interaction and detection with high sensitivity. Considering their facile synthesis procedure and biodegradability, the Au@Fe₃O₄@BCNCs can have a wide range of environmental and biological applications and expected low environmental impacts.

Acknowledgements

Funding for this work was provided through US NSF grants CBET-1705653 and CBET-2029911 to P.V. Laboratory and instrumentation support was provided by NanoEarth a node of the NSF supported NNCI (NSF award number #1542100). Additional support was provided by the Sustainable Nanotechnology Interdisciplinary Graduate Program (VTSuN IGEP) funded by the Virginia Tech Graduate School. Some icons in the graphical abstract were created with BioRender.com.

417 **References**

- 1. Iguchi, M.; Yamanaka, S.; Budhiono, A., Bacterial cellulose—a masterpiece of nature's
- 419 arts. *Journal of materials science* **2000,** *35*, (2), 261-270.
- 420 2. Thomas, B.; Raj, M. C.; Joy, J.; Moores, A.; Drisko, G. L.; Sanchez, C. m., Nanocellulose,
- a versatile green platform: from biosources to materials and their applications. *Chemical reviews*
- **2018,** *118*, (24), 11575-11625.
- 423 3. Wei, H.; Rodriguez, K.; Renneckar, S.; Leng, W.; Vikesland, P. J., Preparation and
- 424 evaluation of nanocellulose–gold nanoparticle nanocomposites for SERS applications. *Analyst*
- 425 **2015**, *140*, (16), 5640-5649.
- 426 4. Carpenter, A. W.; de Lannoy, C.-F.; Wiesner, M. R., Cellulose nanomaterials in water
- 427 treatment technologies. *Environmental science & technology* **2015,** 49, (9), 5277-5287.
- 428 5. Ye, S.; Jiang, L.; Wu, J.; Su, C.; Huang, C.; Liu, X.; Shao, W., Flexible amoxicillin-grafted
- 429 bacterial cellulose sponges for wound dressing: in vitro and in vivo evaluation. ACS applied
- 430 *materials & interfaces* **2018,** *10*, (6), 5862-5870.
- 431 6. Fernandes, S. C.; Sadocco, P.; Alonso-Varona, A.; Palomares, T.; Eceiza, A.; Silvestre, A.
- 432 J.; Mondragon, I. a.; Freire, C. S., Bioinspired antimicrobial and biocompatible bacterial cellulose
- 433 membranes obtained by surface functionalization with aminoalkyl groups. ACS applied materials
- 434 & interfaces **2013**, 5, (8), 3290-3297.
- 435 7. Chen, X.; Xu, X.; Li, W.; Sun, B.; Yan, J.; Chen, C.; Liu, J.; Qian, J.; Sun, D., Effective
- drug carrier based on polyethylenimine-functionalized bacterial cellulose with controllable release
- 437 properties. ACS Applied Bio Materials **2018**, 1, (1), 42-50.
- 438 8. Echeverry Rendon, M.; Reece, L. M.; Pastrana, F.; Arias, S. L.; Shetty, A. R.; Pavón, J.
- 439 J.; Allain, J. P., Bacterial Nanocellulose Magnetically Functionalized for Neuro Endovascular
- 440 Treatment. *Macromolecular bioscience* **2017**, *17*, (6), 1600382.
- Guo, J.; Filpponen, I.; Johansson, L.-S.; Mohammadi, P.; Latikka, M.; Linder, M. B.; Ras,
- 442 R. H.; Rojas, O. J., Complexes of magnetic nanoparticles with cellulose nanocrystals as
- regenerable, highly efficient, and selective platform for protein separation. *Biomacromolecules*
- **2017,** *18*, (3), 898-905.
- Luo, X.; Lei, X.; Cai, N.; Xie, X.; Xue, Y.; Yu, F., Removal of heavy metal ions from water
- by magnetic cellulose-based beads with embedded chemically modified magnetite nanoparticles
- and activated carbon. ACS Sustainable Chemistry & Engineering 2016, 4, (7), 3960-3969.
- 448 11. Laurent, S.; Forge, D.; Port, M.; Roch, A.; Robic, C.; Vander Elst, L.; Muller, R. N.,
- 449 Magnetic iron oxide nanoparticles: synthesis, stabilization, vectorization, physicochemical
- characterizations, and biological applications. *Chemical reviews* **2008**, *108*, (6), 2064-2110.
- 451 12. Teja, A. S.; Koh, P.-Y., Synthesis, properties, and applications of magnetic iron oxide
- anoparticles. Progress in crystal growth and characterization of materials 2009, 55, (1-2), 22-
- 453 45.
- 454 13. Park, M.; Chang, H.; Jeong, D. H.; Hyun, J., Spatial deformation of nanocellulose hydrogel
- 455 enhances SERS. *BioChip Journal* **2013**, *7*, (3), 234-241.

- 456 14. Petryayeva, E.; Krull, U. J., Localized surface plasmon resonance: Nanostructures,
- 457 bioassays and biosensing—A review. *Analytica chimica acta* **2011,** 706, (1), 8-24.
- 458 15. Campion, A.; Kambhampati, P., Surface-enhanced Raman scattering. Chemical Society
- 459 *Reviews* **1998,** *27*, (4), 241-250.
- 460 16. Michaels, A. M.; Nirmal, M.; Brus, L., Surface enhanced Raman spectroscopy of
- individual rhodamine 6G molecules on large Ag nanocrystals. Journal of the American Chemical
- 462 *Society* **1999**, *121*, (43), 9932-9939.
- 463 17. Carrabba, M. M.; Edmonds, R. B.; Rauh, R. D., Feasibility studies for the detection of
- organic surface and subsurface water contaminants by surface-enhanced Raman spectroscopy on
- 465 silver electrodes. *Analytical chemistry* **1987**, *59*, (21), 2559-2563.
- 466 18. Wei, H.; Rodriguez, K.; Renneckar, S.; Vikesland, P. J., Environmental science and
- 467 engineering applications of nanocellulose-based nanocomposites. *Environmental Science: Nano*
- 468 **2014,** *I*, (4), 302-316.
- 469 19. Morales-Narváez, E.; Golmohammadi, H.; Naghdi, T.; Yousefi, H.; Kostiv, U.; Horak, D.;
- 470 Pourreza, N.; Merkoçi, A., Nanopaper as an optical sensing platform. ACS nano 2015, 9, (7), 7296-
- 471 7305.
- 472 20. Habibi, Y.; Goffin, A.-L.; Schiltz, N.; Duquesne, E.; Dubois, P.; Dufresne, A.,
- 473 Bionanocomposites based on poly (ε-caprolactone)-grafted cellulose nanocrystals by ring-opening
- polymerization. *Journal of Materials Chemistry* **2008**, *18*, (41), 5002-5010.
- 475 21. Bossa, N.; Carpenter, A. W.; Kumar, N.; de Lannoy, C.-F.; Wiesner, M., Cellulose
- anocrystal zero-valent iron nanocomposites for groundwater remediation. *Environmental Science*:
- 477 Nano **2017**, 4, (6), 1294-1303.
- 478 22. Brinkmann, A.; Chen, M.; Couillard, M.; Jakubek, Z. J.; Leng, T.; Johnston, L. J.,
- 479 Correlating cellulose nanocrystal particle size and surface area. Langmuir 2016, 32, (24), 6105-
- 480 6114.
- 481 23. Singhsa, P.; Narain, R.; Manuspiya, H., Bacterial cellulose nanocrystals (BCNC)
- 482 preparation and characterization from three bacterial cellulose sources and development of
- functionalized BCNCs as nucleic acid delivery systems. ACS Applied Nano Materials 2017, 1, (1),
- 484 209-221.
- 485 24. George, J.; Kumar, R.; Sajeevkumar, V. A.; Ramana, K. V.; Rajamanickam, R.; Abhishek,
- 486 V.; Nadanasabapathy, S., Hybrid HPMC nanocomposites containing bacterial cellulose
- nanocrystals and silver nanoparticles. *Carbohydrate polymers* **2014**, *105*, 285-292.
- 488 25. Chiang, I. C.; Chen, D. H., Synthesis of monodisperse FeAu nanoparticles with tunable
- 489 magnetic and optical properties. Advanced Functional Materials 2007, 17, (8), 1311-1316.
- 490 26. Wang, J.; Wu, X.; Wang, C.; Rong, Z.; Ding, H.; Li, H.; Li, S.; Shao, N.; Dong, P.; Xiao,
- 491 R., Facile synthesis of Au-coated magnetic nanoparticles and their application in bacteria detection
- 492 via a SERS method. ACS applied materials & interfaces **2016**, 8, (31), 19958-19967.
- 493 27. Saha, D.; Koga, K.; Takeo, H., Stable icosahedral nanoparticles in an as-grown Au–Fe
- 494 alloy. The European Physical Journal D-Atomic, Molecular, Optical and Plasma Physics 1999, 9,
- 495 (1), 539-542.

- 496 28. Lu, D.-l.; Domen, K.; Tanaka, K.-i., Electrodeposited Au– Fe, Au– Ni, and Au– Co Alloy
- Nanoparticles from Aqueous Electrolytes. *Langmuir* **2002**, *18*, (8), 3226-3232.
- 498 29. Long, J.; Yi, H.; Li, H.; Lei, Z.; Yang, T., Reproducible ultrahigh SERS enhancement in
- single deterministic hotspots using nanosphere-plane antennas under radially polarized excitation.
- 500 Scientific reports **2016**, *6*, 33218.
- 30. Qian, X.; Emory, S. R.; Nie, S., Anchoring molecular chromophores to colloidal gold
- 502 nanocrystals: surface-enhanced Raman evidence for strong electronic coupling and irreversible
- structural locking. *Journal of the American Chemical Society* **2012**, *134*, (4), 2000-2003.
- Vasconcelos, N. F.; Feitosa, J. P. A.; da Gama, F. M. P.; Morais, J. P. S.; Andrade, F. K.;
- de Souza, M. d. S. M.; de Freitas Rosa, M., Bacterial cellulose nanocrystals produced under
- different hydrolysis conditions: properties and morphological features. Carbohydrate polymers
- **2017,** *155*, 425-431.
- Roman, M.; Winter, W. T., Effect of sulfate groups from sulfuric acid hydrolysis on the
- thermal degradation behavior of bacterial cellulose. *Biomacromolecules* **2004**, *5*, (5), 1671-1677.
- Wu, X.; Lu, C.; Zhou, Z.; Yuan, G.; Xiong, R.; Zhang, X., Green synthesis and formation
- 511 mechanism of cellulose nanocrystal-supported gold nanoparticles with enhanced catalytic
- 512 performance. Environmental Science: Nano **2014**, 1, (1), 71-79.
- Rashid, M.; Gafur, M. A.; Sharafat, M. K.; Minami, H.; Miah, M. A. J.; Ahmad, H.,
- 514 Biocompatible microcrystalline cellulose particles from cotton wool and magnetization via a
- simple in situ co-precipitation method. *Carbohydrate polymers* **2017**, *170*, 72-79.
- 516 35. He, F.; Zhao, D., Preparation and characterization of a new class of starch-stabilized
- 517 bimetallic nanoparticles for degradation of chlorinated hydrocarbons in water. *Environmental*
- 518 science & technology **2005**, 39, (9), 3314-3320.
- 519 36. Lin, N.; Bruzzese, C. c.; Dufresne, A., TEMPO-oxidized nanocellulose participating as
- crosslinking aid for alginate-based sponges. ACS applied materials & interfaces 2012, 4, (9), 4948-
- 521 4959.
- 522 37. Schwartzberg, A. M.; Grant, C. D.; Wolcott, A.; Talley, C. E.; Huser, T. R.; Bogomolni,
- R.; Zhang, J. Z., Unique gold nanoparticle aggregates as a highly active surface-enhanced Raman
- scattering substrate. The Journal of Physical Chemistry B 2004, 108, (50), 19191-19197.
- 525 38. Deckert Gaudig, T.; Deckert, V., Ultraflat Transparent Gold Nanoplates Ideal
- Substrates for Tip Enhanced Raman Scattering Experiments. *Small* **2009**, *5*, (4), 432-436.
- 527 39. Lin, K.-H.; Hu, D.; Sugimoto, T.; Chang, F.-C.; Kobayashi, M.; Enomae, T., An analysis
- on the electrophoretic mobility of cellulose nanocrystals as thin cylinders: relaxation and end effect.
- 529 RSC Advances **2019**, 9, (58), 34032-34038.
- 530 40. Semenikhin, N. S.; Kadasala, N. R.; Moon, R. J.; Perry, J. W.; Sandhage, K. H.,
- Individually dispersed gold nanoshell-bearing cellulose nanocrystals with tailorable plasmon
- resonance. *Langmuir* **2018**, *34*, (15), 4427-4436.
- 533 41. Csapó, E.; Sebők, D.; Makrai Babić, J.; Šupljika, F.; Bohus, G.; Dékány, I.; Kallay, N.;
- Preočanin, T., Surface and structural properties of gold nanoparticles and their biofunctionalized
- derivatives in aqueous electrolytes solution. Journal of dispersion science and technology 2014,
- *35*, (6), 815-825.

- Lueck, H. B.; Daniel, D. C.; McHale, J. L., Resonance Raman study of solvent effects on
- a series of triarylmethane dyes. *Journal of Raman spectroscopy* **1993,** 24, (6), 363-370.
- 539 43. Li, M.; Zhang, J.; Suri, S.; Sooter, L. J.; Ma, D.; Wu, N., Detection of adenosine
- 540 triphosphate with an aptamer biosensor based on surface-enhanced Raman scattering. *Analytical*
- 541 *chemistry* **2012,** *84*, (6), 2837-2842.
- 542 44. Wei, H.; Leng, W.; Song, J.; Willner, M. R.; Marr, L. C.; Zhou, W.; Vikesland, P. J.,
- 543 Improved quantitative SERS enabled by surface plasmon enhanced elastic light scattering.
- 544 Analytical chemistry **2018**, 90, (5), 3227-3237.
- 545 45. Wei, H.; Huang, Q.; Vikesland, P. J., The Aromatic Amine p K a Determines the Affinity
- for Citrate-Coated Gold Nanoparticles: In Situ Observation via Hot Spot-Normalized Surface-
- Enhanced Raman Spectroscopy. Environmental Science & Technology Letters 2019, 6, (4), 199-
- 548 204.
- 549 46. Wei, H.; Leng, W.; Song, J.; Liu, C.; Willner, M. R.; Huang, Q.; Zhou, W.; Vikesland, P.
- J., Real-time monitoring of ligand exchange kinetics on gold nanoparticle surfaces enabled by hot
- spot-normalized surface-enhanced Raman scattering. Environmental science & technology 2018,
- *552 53*, (2), 575-585.
- Wei, H.; McCarthy, A.; Song, J.; Zhou, W.; Vikesland, P. J., Quantitative SERS by hot
- 554 spot normalization-surface enhanced Rayleigh band intensity as an alternative evaluation
- parameter for SERS substrate performance. Faraday discussions 2017, 205, 491-504.
- 556 48. Dinish, U.; Balasundaram, G.; Chang, Y. T.; Olivo, M., Sensitive multiplex detection of
- serological liver cancer biomarkers using SERS active photonic crystal fiber probe. *Journal of*
- 558 biophotonics **2014,** 7, (11 12), 956-965.
- 559 49. Kowalska, A.; Kaminska, A.; Adamkiewicz, W.; Witkowska, E.; Tkacz, M., Novel
- 560 highly sensitive Cu based SERS platforms for biosensing applications. Journal of Raman
- 561 *spectroscopy* **2015,** *46*, (5), 428-433.
- 562 50. Wu, Z.; Liu, Y.; Zhou, X.; Shen, A.; Hu, J., A "turn-off" SERS-based detection platform
- for ultrasensitive detection of thrombin based on enzymatic assays. *Biosensors and Bioelectronics*
- **2013,** *44*, 10-15.
- 565 51. Bao, Z. Y.; Liu, X.; Chen, Y.; Wu, Y.; Chan, H. L.; Dai, J.; Lei, D. Y., Quantitative SERS
- detection of low-concentration aromatic polychlorinated biphenyl-77 and 2, 4, 6-trinitrotoluene.
- *Journal of hazardous materials* **2014,** *280*, *706-712*.
- 568 52. Yang, S.; Dai, X.; Stogin, B. B.; Wong, T.-S., Ultrasensitive surface-enhanced Raman
- scattering detection in common fluids. Proceedings of the National Academy of Sciences 2016,
- 570 *113*, (2), 268-273.
- 571 53. Shrivastava, A.; Gupta, V. B., Methods for the determination of limit of detection and limit
- of quantitation of the analytical methods. *Chronicles of young scientists* **2011**, *2*, (1), 21.
- 573 54. Robinson, I.; Tung, L. D.; Maenosono, S.; Wälti, C.; Thanh, N. T., Synthesis of core-shell
- gold coated magnetic nanoparticles and their interaction with thiolated DNA. *Nanoscale* **2010**, *2*,
- 575 (12), 2624-2630.